Article

Atomic Bose–Einstein condensate in twisted-bilayer optical lattices

https://doi.org/10.1038/s41586-023-05695-4

Received: 11 October 2021

Accepted: 3 January 2023

Published online: 22 February 2023

Check for updates

Zengming Meng[1,5], Liangwei Wang[1,5], Wei Han[1], Fangde Liu[1], Kai Wen[1], Chao Gao[2], Pengjun Wang[1], Cheng Chin[3] & Jing Zhang[1,4]✉

Observation of strong correlations and superconductivity in twisted-bilayer graphene[1–4] has stimulated tremendous interest in fundamental and applied physics[5–8]. In this system, the superposition of two twisted honeycomb lattices, generating a moiré pattern, is the key to the observed flat electronic bands, slow electron velocity and large density of states[9–12]. Extension of the twisted-bilayer system to new configurations is highly desired, which can provide exciting prospects to investigate twistronics beyond bilayer graphene. Here we demonstrate a quantum simulation of superfluid to Mott insulator transition in twisted-bilayer square lattices based on atomic Bose–Einstein condensates loaded into spin-dependent optical lattices. The lattices are made of two sets of laser beams that independently address atoms in different spin states, which form the synthetic dimension accommodating the two layers. The interlayer coupling is highly controllable by a microwave field, which enables the occurrence of a lowest flat band and new correlated phases in the strong coupling limit. We directly observe the spatial moiré pattern and the momentum diffraction, which confirm the presence of two forms of superfluid and a modified superfluid to insulator transition in twisted-bilayer lattices. Our scheme is generic and can be applied to different lattice geometries and for both boson and fermion systems. This opens up a new direction for exploring moiré physics in ultracold atoms with highly controllable optical lattices.

New band structures in lattice systems often lead to new material functions and discoveries. Twistronics, originating from the twisted-bilayer-graphene as a tuneable experimental platform[1–8], has attracted broad attention in recent years and launched intensive theoretical research. Here, overlaying two graphene layers with a small relative angle show the rich phase diagram, such as the coexistence of unconventional superconductivity and correlated insulating phases[2–4]. In recent years, many examples of twisted-bilayer are discovered with remarkable physical properties not present in their untwisted counterparts. Recently, photonic moiré lattices are explored for their capabilities in localizing and delocalizing light[13–15] and engineering the photonic dispersion of phonon polaritons[16].

Ultracold atoms in optical lattices constitute an ideal platform to simulate emerging many-body phenomena in condensed matter physics[17–19]. Different optical lattice geometries can be realized by interfering different sets of laser beams[20–25]. In particular, a scheme of simulating twisted-bilayer lattice has recently been proposed using two overlapping optical lattices[26,27]. Other schemes for simulating bilayer heterostructures have also been put forward[28,29]. These schemes are based on coherent coupling between spin states of atoms, which simulates interlayer tunnelling along an artificial, synthetic dimension[30–32].

In this article, we demonstrate Bose–Einstein condensates (BEC) of Rubidium-87 (^{87}Rb) atoms loaded into a pair of twisted-bilayer optical lattices. Two overlapping lattices V_1 and V_2 are formed by interfering laser beams at the specific 'tune-out' wavelengths[33–35] λ_1 and λ_2 with proper polarizations such that atoms in spin state $|1\rangle \equiv |F=1, m_F=1\rangle$ and state $|2\rangle \equiv |F=2, m_F=0\rangle$ only experience the lattice potential V_1 and V_2, respectively (Fig. 1). Here F and m_F are the angular momentum and projection quantum numbers in the ^{87}Rb ground state manifold. Each set of the laser beams forms a two-dimensional (2D) square lattice on the horizontal xy plane and the twist of the two lattices is realized by orienting the beams of different wavelengths with a small relative angle $\theta = 5.21°$. The sample is tightly confined in the vertical z direction such that the sample is in the quasi-2D regime (see Methods for details).

The two spin states of ^{87}Rb atoms constitute the synthetic dimension that accommodates the two twisted layers of lattices V_1 and V_2. To precisely determine the tune-out wavelengths λ_1 and λ_2 of the optical lattices V_1 and V_2, we measure the diffraction of atoms by the optical lattices. The experimental sequence starts with an almost pure BEC in a crossed-beam dipole trap. The atoms are prepared in one of the two spin states and a short pulse of the lattice beams is applied. The lattice potential induces Bragg diffraction of atoms to high momentum states. After turning off the lattice beams, we image the diffracted atoms. The wavelengths of the lattice beams are finely adjusted to the tune-out wavelengths such that atoms in state $|1\rangle$ are only diffracted by the lat-

[1]State Key Laboratory of Quantum Optics and Quantum Optics Devices, Institute of Opto-Electronics, Collaborative Innovation Center of Extreme Optics, Shanxi University, Taiyuan, P. R. China. [2]Department of Physics, Zhejiang Normal University, Jinhua, P. R. China. [3]James Franck Institute, Enrico Fermi Institute, Department of Physics, University of Chicago, Chicago, IL, USA. [4]Hefei National Laboratory, Hefei, P. R. China. [5]These authors contributed equally: Zengming Meng, Liangwei Wang. ✉e-mail: jzhang74@sxu.edu.cn

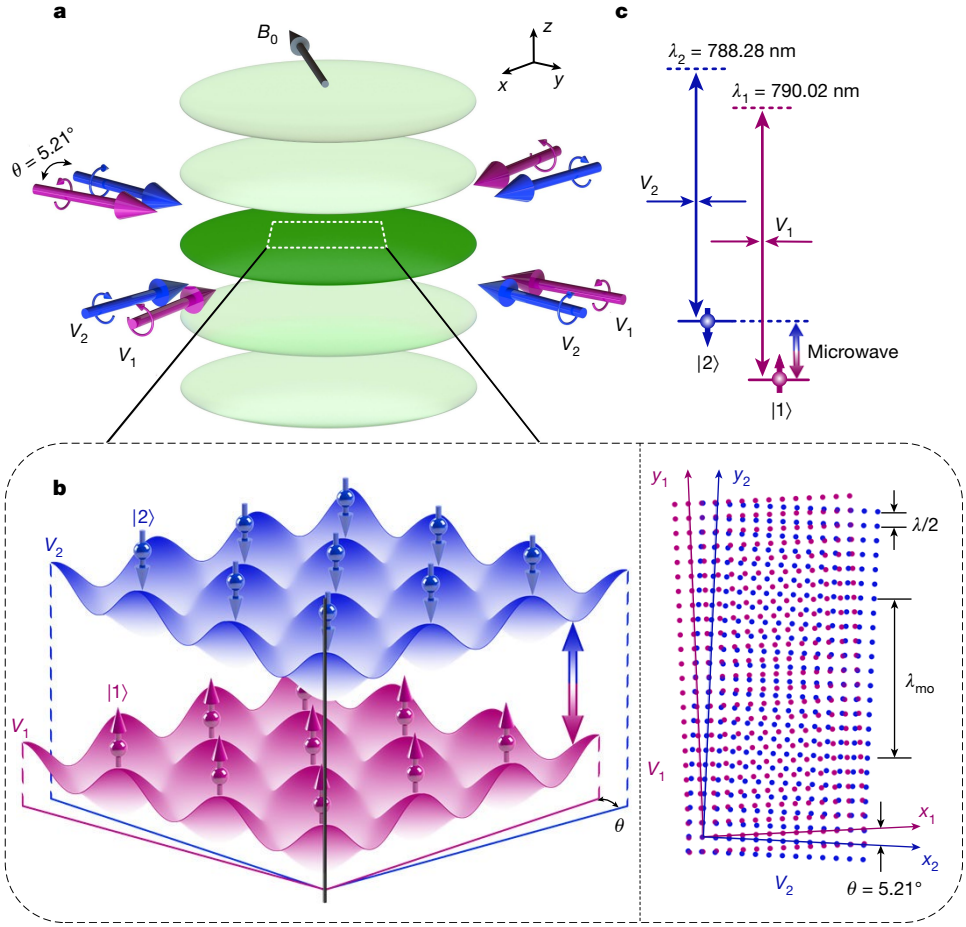

Fig. 1 | Simulation of twisted-bilayer systems based on atoms in spin-dependent optical lattices. a, Atoms are loaded into a single layer, 2D pancake-like potential formed by a vertical optical lattice (green) in the z direction. Two sets of square optical lattices V_1 (purple) and V_2 (blue) on the horizontal plane with a small relative angle $\theta = 5.21°$ form a spin-dependent lattice potential and confine Rb atoms in spin state $|1\rangle$ (up arrows) and $|2\rangle$ (down arrows) independently. A magnetic field is applied in the xy plane along the 45° diagonal of the V_2 lattice. The lattice beams for V_1 and V_2 are set with opposite circular polarization to generate the vector shift with the opposite sign. **b**, The left panel shows a sketch of the bilayer lattices in the synthetic dimension. The interlayer tunnelling is controlled by a microwave field. The right panel shows a superimposed lattice structure with the lattice constant $\lambda/2$ and much larger moiré length λ_{mo}. **c**, Energy diagram of the two ground Zeeman states $|1\rangle$ and $|2\rangle$ and the associated lattice beams at the tune-out wavelengths $\lambda_1 = 790.02$ and $\lambda_2 = 788.28$ nm.

tice potential V_1 and not by the potential V_2 as shown in Fig. 2. Similarly, atoms in state $|2\rangle$ only experience the potential V_2, but not V_1. By eliminating the cross-talks, we determined the tune-out wavelengths to be $\lambda_1 = 790.02$ and $\lambda_2 = 788.28$ nm. The lattice beams are circularly polarized to produce spatial intensity modulation such that the lattice potentials are attractive to atoms in both spin states (see Methods for details).

Experimentally intralayer hoppings t_1 and t_2 between lattice sites are controlled by the depth of the optical lattices V_1 and V_2; interlayer hopping Ω_R, on the other hand, is independently induced by microwaves (MW) that couple the two spin states. Starting with atoms in state $|1\rangle$ in the dipole trap, for example, the MW spectrum shows a single narrow peak when atoms are driven to state $|2\rangle$. By loading the atoms into the twisted-bilayer optical lattices, the spectrum shows several peaks. The peaks correspond to transitions from atoms in the ground band of lattice V_1, which we label $|1, S\rangle$, to different Bloch bands of lattice V_2, which we label $|2, S\rangle$, $|2, P\rangle$, $|2, D\rangle$ and so on (Fig. 3a,b). The peak locations agree with the calculated energies of the s, p and d bands in lattice V_2. The multi-peak structure supports that atoms in different spin states are confined in different lattices. If atoms are loaded into a spin-independent lattice, only a single narrow peak shows up in the spectrum, which belongs to the $|1, S\rangle$ to $|2, S\rangle$ transition. This is because MW transitions between different Bloch bands are negligible in spin-independent lattices. In the twisted optical lattice, the transitions from the s band of state $|1\rangle$ to other bands of state $|2\rangle$ are allowed. In the presence of the twisted-bilayer lattices, the transitions are broadened as the two spin states experience different trap potentials, which induce fast dephasing. Moreover, the on-site interactions increase in deeper lattice potential, resulting in faster decay from high bands to lower bands and thus broader spectral lines. Our observation supports MW as a versatile and powerful tool to induce interlayer hopping between the two twisted layers in the synthetic (spin) dimension.

To quantify the interlayer hopping energy, we measure the time evolution of the population in state $|2\rangle$. We observe a coherent oscillation at detuning $\Delta = -0.9$ kHz, which corresponds to the transition from $|1, S\rangle$ to $|2, S\rangle$ (Fig. 3c). The interlayer coupling strength can be determined from the oscillation frequencies. In our experiment, the coupling strength is tuneable up to $1E_r$, which exceeds that in typical twisted-bilayer graphene systems. On the other hand, coupling to the p band $|2, P\rangle$ leads to faster decay probably due to collisional relaxation to the lower s band (Fig. 3d). In the following, we will focus on atoms in the twisted-bilayer optical lattices with MW-induced coupling between the s bands of the two layers.

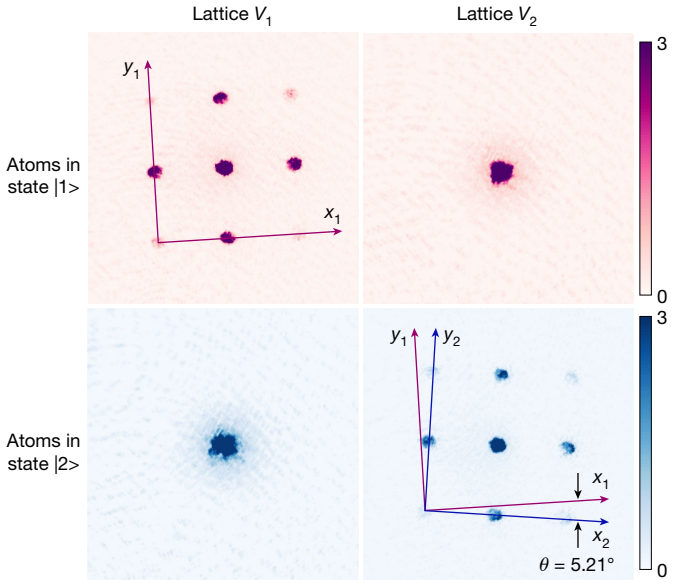

Fig. 2 | Independent diffraction of atoms in different spin states by the twisted-bilayer optical lattices. The optical lattice potential is applied to the atomic BEC with a short duration of 4 μs. The images show diffraction patterns of the atoms after 18 ms of free space expansion. At the tune-out wavelength $\lambda_1 = 790.02$ and $\lambda_2 = 788.28$ nm, atoms in state $|1\rangle$ and $|2\rangle$, are diffracted by the associated optical lattices V_1 and V_2, respectively.

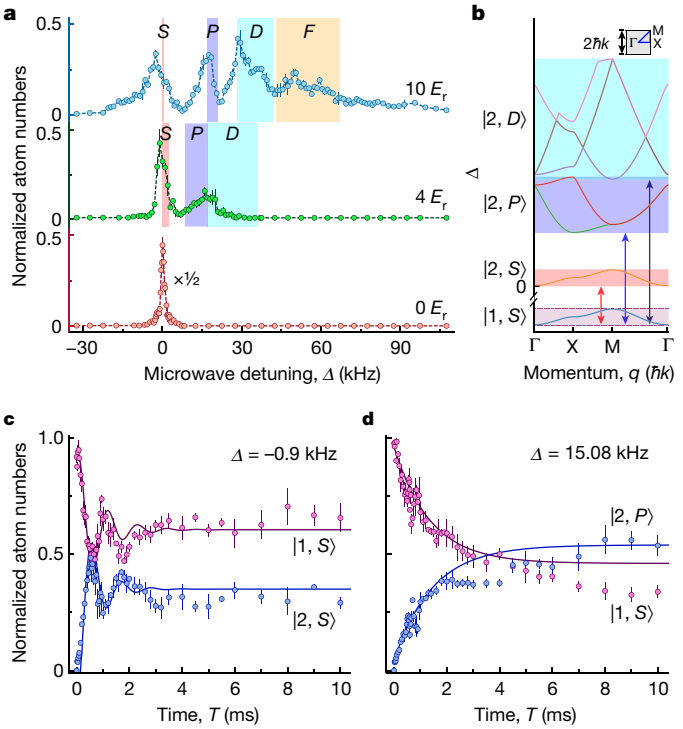

Fig. 3 | Interlayer coupling in twisted-bilayer optical lattices. a, MW spectrum of atoms in the twisted-bilayer optical lattices. Atoms in spin state $|1\rangle$ are driven by MW to spin state $|2\rangle$ in the presence of the lattice potential with depth of 0 (no lattice), 4 and $10E_r$. Here $E_r = q_r^2/2m = h \times 3.67$ kHz is the recoil energy, $q_r = \hbar k = h/\lambda$ is the recoil momentum, m is the atomic mass of ^{87}Rb and λ is the wavelength of the lattice laser. The MW pulse length of 530 μs corresponds to a π pulse in the absence of the lattice potential. **b**, Lattice band structure for the two spin states calculated with the lattice depth $4E_r$. The MW field drives atoms from the s band of state $|1\rangle$, labelled as $|1, S\rangle$ to s, p and d bands of state $|2\rangle$ with different detuning Δ. **c**,**d**, Starting with all atoms in $|1, S\rangle$, population in state $|2\rangle$ is measured in the twisted-bilayer lattices at $4E_r$ after the MW pulse that drives the atoms to $|2, S\rangle$ with the detuning $\Delta = -0.9$ kHz (**c**), or to $|2, P\rangle$ with detuning $\Delta = 15.08$ kHz (**d**). Fits in **c** show an interlayer coupling frequency of $\Omega_R = 2\pi \times 893$ Hz and a decay rate of 1,200 s^{-1}. Lines in **d** are guides to the eye. Each point is based on three or more measurements and error bars show the standard deviations of the mean.

A key signature of atoms in the twisted-bilayer optical lattice is the moiré lattice with a period

$$\lambda_{mo} = \frac{a}{2\sin\theta/2}, \quad (1)$$

which, for the lattice constant $a = 395$ nm and twist angle $\theta = 5.21°$, amounts to a moiré length $\lambda_{mo} = 4.35$ μm. The large moiré period gives rise to a mini-Brillouin zone in the momentum space, which is expected to generate the flat bands and strongly correlated states[1–12]. Notably, an in situ moiré pattern is also observed in one-dimensional lattices with two lattice constants[36]. To identify the moiré length scale in our system, we use in situ absorption imaging to visualize the moiré pattern (Fig. 4a–f). Here we first load the atoms in state $|1\rangle$ into the lowest s band of lattice V_1 and then ramp up the MW field with detuning $\Delta = -0.9$ kHz to drive the transition from $|1, S\rangle$ to $|2, S\rangle$. We then in situ image the atoms in state $|2\rangle$. Moiré patterns in one and two dimensions are observed, and the moiré period is measured to be 4.35 μm consistent with expectation (Fig. 4a–f). Note that the primary optical lattice spacing $a = 395$ nm is indiscernible with our imaging optics.

We also examine the quantum state of atoms in the bilayer twisted lattices by analysing their momentum-space distribution. After loading a BEC into the bilayer lattice of $4E_r$ in the presence of resonant MW transition, we hold for some time and then perform the time-of-flight (TOF) measurement (Fig. 4g,h). Two sets of diffractions manifest, which correspond to the primary lattice momentum π/a and the much smaller moiré momentum π/λ_{mo}. The high contrast of both sets of diffraction pattern suggests that the atoms remain in the superfluid phase with phase coherence extending beyond the moiré length scale. In particular, the contrasts of the moiré pattern in real and momentum space persist over 40 ms (Fig. 4i), from which we conclude that the atoms maintain in the superfluid phase in the twisted-bilayer lattices.

Theoretically, depending on the twist angle θ, the superimposed twisted-bilayer lattice can yield either a periodic potential with supercells that supports a delocalized ground state or a quasi-periodic one that supports a localized ground state in the absence of interactions. In fact, only specific twist angles give rise to periodic lattice potentials. For square lattices, the twist angles that lead to commensurate superlattice should satisfy $\theta = 2\arctan(\overline{m}/\overline{n})$, where $\overline{m}$ and $\overline{n}$ are coprime natural number[13]. The twist angle $\theta = 5.21°$ used in our work is close to the commensurate angle $\theta = 2\arctan(1/22) \approx 5.205°$, and the period of the supercell is given by $2\lambda_{mo} \approx 22a$ (see Methods for details). Whereas our twist angle does not exactly match the commensurate angle $\theta = 2\arctan(1/22) \approx 5.205°$, the small difference cannot be distinguished in a finite size sample due to repulsive interactions (see Methods for details). In particular, the spatial moiré period remains a clear observable in our experiment because of the finite chemical potential of our atomic superfluid. The persistence of the spatial and momentum periodicity of the sample in the twisted-bilayer lattice supports the superfluid as the ground state of the system.

Compared with electronic materials, in which the flat band is investigated frequently near the Fermi surface, we can also explore flat-band physics with bosons condensed in the lowest band. In our system, when interlayer coupling increases, the long-wavelength moiré potential becomes deeper, so atoms in the lowest band are isolated at a larger spatial scale (moiré wavelength), which flattens the ground band and

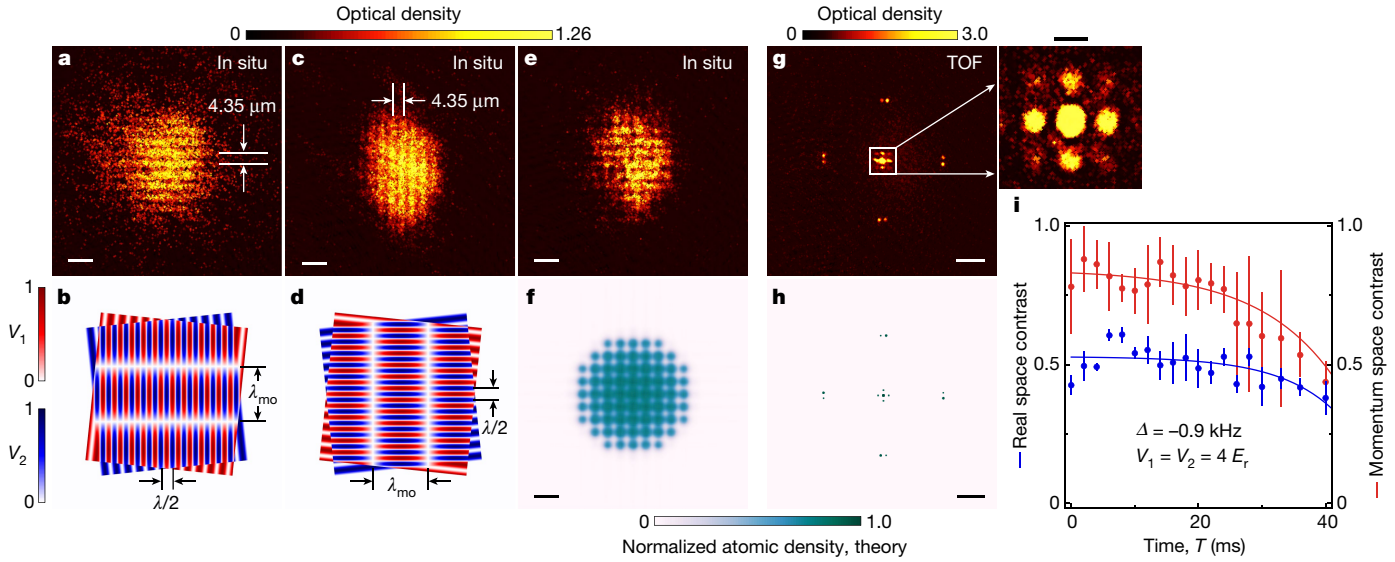

Fig. 4 | Moiré pattern and superfluid ground state in twisted-bilayer optical lattices. a,**c**, Moiré pattern of atoms in one-dimensional bilayer optical lattices in the x (**a**) and y directions (**c**). **b**,**d**, Plot of the corresponding optical lattice potential in the x (**b**) and y directions (**d**). Note that the primary optical lattice $\lambda/2$ is indiscernible in the in situ images. In all experiments, an MW field is applied to couple the s band of state $|1\rangle$ and s band of state $|2\rangle$. The atoms in state $|2\rangle$ are measured. The elliptical shape of the atomic cloud is induced by a little asymmetric harmonic trap potential in xy plane. **e**,**f**, Experimental (**e**) and theoretical (**f**) moiré pattern of atoms in the presence of optical lattices in both directions. **g**,**h**, TOF images with 18 ms from the experiment (**g**) and calculation (**h**) show diffraction peaks associated with the primary lattice constant $\lambda/2$ and moiré length λ_{mo}. The enlarged picture of the centre part of **g** is obtained by the imaging system with higher magnification. **i**, The contrast of moiré pattern in real space and the contrast of diffraction pattern for different hold times. Here, the lattice depths are $V_{1x} = V_{2x} = V_{1y} = V_{2y} = 4E_r$ ($U/t = 1.67$, $\Omega_R/t = 2.07$, U is the on-site interaction). The real-space and momentum-space distributions of **f** and **h** are theoretically calculated by solving the mean-field ground states according to the Gross–Pitaevskii equations (see Methods for details). The contrast in the real space is defined as $(S_{max} - S_{min})/(S_{max} + S_{min})$, where S_{max} and S_{min} are the maximum and minimum atomic density of the moiré fringes. The contrast in the momentum space is defined as $(P^{av}_{max} - P_{min})/(P^{av}_{max} + P_{min})$, where, $P^{av}_{max} = (P^0_{max} + P^1_{max})/2$ and P_{min} are the average maximum and minimum density of the diffraction pattern. Here P^0_{max} is zero-momentum component and P^1_{max} is the moiré component near the zero momentum. Error bars show the standard deviation of the mean. Scale bars **a**,**c**,**e**,**f**, 10 μm, **g**,**h**, 100 μm and inset of **g**, 20 μm.

enhances the localization of the atoms. In the large interlayer coupling limit, the system can be regarded as a single layer (single-component) experiencing a twisted optical lattice (see Methods for details). The single-layer system with a twisted optical lattice admits a flat-band structure in the ground band, which has also been studied experimentally in photonic systems[13–15]. The easily tuned intra- and interlayer couplings in our system offer the added advantages of seeking new quantum phases and phase transitions with cold atoms.

By varying the depth of optical lattices and interlayer coupling, we find several distinct quantum phases, including superfluid (SF), superfluid with only short-range coherence (SF-II), Mott insulator (MI) and insulator (I) (Fig. 5a and Methods). These phases can be distinguished

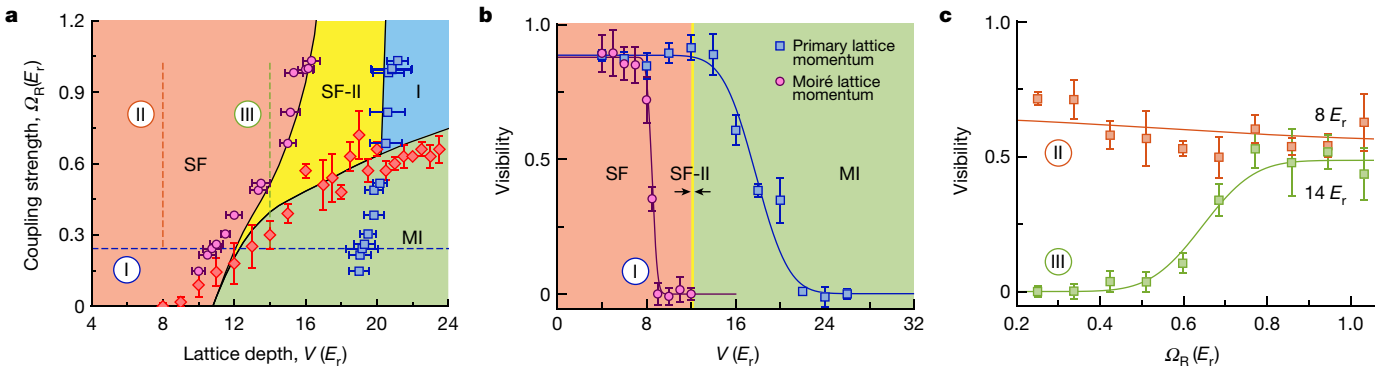

Fig. 5 | Phase transition for the twisted-bilayer optical lattice. a, Phase diagram (see Methods for details), in which SF, SF-II, MI and I refer to superfluid, superfluid only with short-range coherence, Mott insulator and insulator. The solid curves denote the calculated phase boundaries with mean-field at zero temperature. The dots are experimental measurements of the phase boundaries. The pink circles and blue squares denote the loss of the coherence at the moiré length scale and the length scale of the primary lattice, respectively. The red diamonds denote the appearance of the moiré pattern in the real-space in situ images that increases the interlayer coupling. The error bars indicate the experimental uncertainties in determining the phase transition. **b**, Visibility curves for the moiré and primary lattice momentum components as a function of lattice depth (path I in **a**). A sequential loss of phase coherence appears at the moiré momentum and the primary lattice momentum. The intermediate regime indicates SF-II phase. The interlayer coupling frequency is $\Omega_R = 0.24E_r$. **c**, Visibility curves for the moiré momentum component as a function of interlayer coupling with the lattice depth $8E_r$ (path II in **a**) and $14E_r$ (path III in **a**), respectively. The solid lines in **b** and **c** are fitted from the experimental data and only guide the eye.

by the phase coherence and real-space density correlations. The SF-II phase emerges with finite interlayer coupling around the transition from a regular SF to an insulator. The spatial range of phase coherence is the key to distinguishing the two SF phases: while an SF supports long-range phase coherence[37], the SF-II phase maintains the coherence only up to the moiré length scale. In addition, the SF-II phase supports the moiré pattern in the real space. Theoretically, SF-II is the phase with superfluid domains embedded in a gapped insulator, induced by the interlayer coupling. Finally, the insulator phases I and MI can be identified by the disappearance of spatial coherence at all scales and integer fillings of all the sites. Whereas the MI has uniform atom density with weak interlayer coupling, the I phase features a moiré pattern due to stronger interlayer coupling.

In the experiment, we measure the phase coherence from the momentum-space diffraction peaks in the TOF images and directly probe the moiré pattern by in situ imaging following the measurement method as shown in Fig. 4. The measurement of the phase boundaries is shown in Fig. 5a. We use three independent paths to study these phases. In path I, we fix the interlayer coupling strength at a small value $\Omega_R = 0.24E_r$ and increase the lattice depth. The phase transition from SF to MI and across SF-II is shown in the TOF images (Fig. 5b). Here the diffraction peaks at the moiré momenta disappear first before the disappearance of the primary lattice. The intermediate regime indicates the SF-II phase in which the moiré-scale long-range correlation is destroyed while a short-range coherence remains; at the same time, the density correlations of moiré pattern appear in the real space. In path II, we fix the lattice depth in the SF region and increase the interlayer coupling. The diffraction peaks at the moiré momenta persist with high contrasts. However, in path III, when the depth of optical lattices is fixed at the MI region and the interlayer coupling increases, the visibility at the moiré momenta presents the threshold behaviour and emerges at $\Omega_R > 0.5E_r$ (Fig. 5c). These observations are qualitatively consistent with the theoretical expectation and demonstrate that the interlayer coupling can induce a re-entrant transition from MI to SF across SF-II. One may understand such rich transitions from the fact that the interplay between the interlayer coupling and interactions tends to localize the bosons, primarily in the moiré length scale.

This work provides a preliminary physical insight into the quantum phase transition between SF and SF-II (MI and SF-II or MI and I) and offers the possibility to study the complex phases due to the presence of quasi-disorder induced by large interlayer coupling and strong interaction, such as Bose glass insulator, resembling that in disordered bosonic systems[38–40]. These complex phases are worth further investigating in the future.

The present work focuses on the realization and the ground state properties of atoms in the twisted-bilayer optical square lattice. Our success in loading a superfluid into the bilayer lattice demonstrates a new versatile platform to explore moiré physics and the associated superfluidity in a quantum many-body system. Beyond the tuneable twist angle, the cold atom platform offers remarkable controls such as different lattice depths and interlayer coupling in different layers.

Furthermore, the twisted-bilayer square lattice closely connects to the physics of heterostructures of twisted atomically thin semiconductors[8,41,42]. At the same time, our experiment can in principle be extended to multi-layer lattice in which the interlayer couplings can be independently induced by MW and radio-frequencies. Replacing the MW with optical Raman transitions, the interlayer coupling can be spatial dependence, which can support topological ground states. Finally, our optical lattice scheme can be applied to confine fermionic atoms in bilayer hexagonal lattice, which faithfully simulates electrons in a bilayer graphene, and may offer insight into the emergence of superconductivity in the strongly correlated, flat-band regime.

Online content

Any methods, additional references, Nature Portfolio reporting summaries, source data, extended data, supplementary information, acknowledgements, peer review information; details of author contributions and competing interests; and statements of data and code availability are available at https://doi.org/10.1038/s41586-023-05695-4.

1. Cao, Y. et al. Correlated insulator behaviour at half-filling in magic-angle graphene superlattices. *Nature* **556**, 80–84 (2018).
2. Cao, Y. et al. Unconventional superconductivity in magic-angle graphene superlattices. *Nature* **556**, 43–50 (2018).
3. Yankowitz, M. et al. Tuning superconductivity in twisted bilayer graphene. *Science* **363**, 1059–1064 (2019).
4. Lu, X. et al. Superconductors, orbital magnets and correlated states in magic-angle bilayer graphene. *Nature* **574**, 653–657 (2019).
5. Wang, J., Mu, X., Wang, L. & Sun, M. Properties and applications of new superlattice: twisted bilayer graphene. *Mater. Today Phys.* **9**, 100099 (2019).
6. Andrei, E. Y. & MacDonald, A. H. Graphene bilayers with a twist. *Nat. Mater.* **19**, 1265–1275 (2020).
7. Balents, L., Dean, C. R., Efetov, D. K. & Young, A. F. Superconductivity and strong correlations in Moiré flat bands. *Nat. Phys.* **16**, 725–733 (2020).
8. Kennes, D. M. et al. Moiré heterostructures as a condensed-matter quantum simulator. *Nat. Phys.* **17**, 155–163 (2021).
9. Lopes dos Santos, J. M. B., Peres, N. M. R. & Castro Neto, A. H. Graphene bilayer with a twist: electronic structure. *Phys. Rev. Lett.* **99**, 256802 (2007).
10. Mele, E. J. Commensuration and interlayer coherence in twisted bilayer graphene. *Phys. Rev. B* **81**, 161405 (2010).
11. Bistritzer, R. & MacDonald, A. H. Moiré bands in twisted double-layer graphene. *Proc. Natl Acad. Sci. USA* **108**, 12233–12237 (2011).
12. Moon, P. & Koshino, M. Energy spectrum and quantum Hall effect in twisted bilayer graphene. *Phys. Rev. B* **85**, 195458 (2012).
13. Wang, P. et al. Localization and delocalization of light in photonic moiré lattices. *Nature* **577**, 42–46 (2020).
14. Huang, C. et al. Localization-delocalization wavepacket transition in Pythagorean aperiodic potentials. *Sci. Rep.* **6**, 32546 (2016).
15. Fu, Q. et al. Optical soliton formation controlled by angle twisting in photonic Moiré lattices. *Nat. Photon.* **14**, 663–668 (2020).
16. Hu, G. et al. Topological polaritons and photonic magic angles in twisted α-MoO_3 bilayers. *Nature* **582**, 209–213 (2020).
17. Bloch, I., Dalibard, J. & Zwerger, W. Many-body physics with ultracold gases. *Rev. Mod. Phys.* **80**, 885–964 (2008).
18. Lewenstein, M., Sanpera, A. & Ahufinger, V. *Ultracold Atoms in Optical Lattices: Simulating Quantum Many-Body systems* (Oxford Univ. Press, 2012).
19. Windpassinger, P. & Sengstock, K. Engineering novel optical lattices. *Rep. Prog. Phys.* **76**, 086401 (2013).
20. Soltan-Panahi, P. et al. Multi-component quantum gases in spin-dependent hexagonal lattices. *Nat. Phys.* **7**, 434–440 (2011).
21. Wirth, G., Ölschläger, M. & Hemmerich, A. Evidence for orbital superfluidity in the P-band of a bipartite optical square lattice. *Nat. Phys.* **7**, 147–153 (2011).
22. Tarruell, L., Greif, D., Uehlinger, T., Jotzu, G. & Esslinger, T. Creating, moving and merging Dirac points with a Fermi gas in a tunable honeycomb lattice. *Nature* **483**, 302–305 (2012).
23. Jo, G. B. et al. Ultracold atoms in a tunable optical kagome lattice. *Phys. Rev. Lett.* **108**, 045305 (2012).
24. Taie, S. et al. Coherent driving and freezing of bosonic matter wave in an optical Lieb lattice. *Sci. Adv.* **1**, e1500854 (2015).
25. Gall, M., Wurz, N., Samland, J., Chan, C. F. & Köhl, M. Competing magnetic orders in a bilayer Hubbard model with ultracold atoms. *Nature* **589**, 40 (2021).
26. González-Tudela, A. & Cirac, J. I. Cold atoms in twisted-bilayer optical potentials. *Phys. Rev. A* **100**, 053604 (2019).
27. Luo, X. & Zhang, C. Spin-twisted optical lattices: tunable flat bands and Larkin-Ovchinnikov superfluids. *Phys. Rev. Lett.* **126**, 103201 (2021).
28. Graß, T., Chhajlany, R. W., Tarruell, L., Pellegrini, V. & Lewenstein, M. Proximity effects in cold atom artificial graphene. *2D Mater.* **4**, 015039 (2016).
29. Salamon, T. et al. Simulating twistronics without a twist. *Phys. Rev. Lett.* **125**, 030504 (2020).
30. Boada, O., Celi, A., Latorre, J. I. & Lewenstein, M. Quantum simulation of an extra dimension. *Phys. Rev. Lett.* **108**, 133001 (2012).
31. Celi, A. et al. Synthetic gauge fields in synthetic dimensions. *Phys. Rev. Lett.* **112**, 043001 (2014).
32. Ozawa, T. & Price, H. M. Topological quantum matter in synthetic dimensions. *Nat. Rev. Phys.* **1**, 349–357 (2019).
33. LeBlanc, L. J. & Thywissen, J. H. Species-specific optical lattices. *Phys. Rev. A* **75**, 053612 (2007).
34. Arora, B., Safronova, M. S. & Clark, C. W. Tune-out wavelengths of alkali-metal atoms and their applications. *Phys. Rev. A* **84**, 043401 (2011).
35. Wen, K. et al. Experimental study of tune-out wavelengths for spin-dependent optical lattice in ^{87}Rb Bose-Einstein condensation. *J. Opt. Soc. Am. B* **38**, 3269 (2021).
36. McDonald, M., Trisnadi, J., Yao, K. & Chin, C. Superresolution microscopy of cold atoms in an optical lattice. *Phys. Rev. X* **9**, 021001 (2019).
37. Gerbier, F. et al. Interference pattern and visibility of a Mott insulator. *Phys. Rev. A* **72**, 053606 (2005).

38. Fisher, M. P. A., Weichman, P. B., Grinstein, G. & Fisher, D. S. Boson localization and the superfluid-insulator transition. *Phys. Rev. B* **40**, 546–570 (1989).
39. Krauth, W., Trivedi, N. & Ceperley, D. Superfluid-insulator transition in disordered boson systems. *Phys. Rev. Lett.* **67**, 2307–2310 (1991).
40. Freericks, J. K. & Monien, H. Strong-coupling expansions for the pure and disordered Bose-Hubbard model. *Phys. Rev. B* **53**, 2691–2700 (1996).
41. Kariyado, T. & Vishwanath, A. Flat band in twisted bilayer Bravais lattices. *Phys. Rev. Res.* **1**, 033076 (2019).
42. Kennes, D. M., Xian, L., Claassen, M. & Rubio, A. One-dimensional flat bands in twisted bilayer germanium selenide. *Nat. Commun.* **11**, 31124 (2020).

Methods

Experimental setup

In our experiment, the ultracold ^{87}Rb atoms in the $|F=2, m_F=2\rangle$ state are prepared in the crossed optical dipole trap[43]. Forced evaporation in the optical trap creates the BEC with up to 5×10^5 atoms. The atoms can be transferred to the $|F=1, m_F=1\rangle$ state through a rapid adiabatic passage induced by MW transition. To load the atoms into the 2D trap, a 532 nm laser beam is deflected by an acousto-optic deflector and then split into two beams with variable spacing adjusted by the acousto-optic deflector. The two beams are focused onto the atoms with a 150 mm aspherical lens. These beams interfere to form a standing wave in the vertical direction with variable separation (accordion lattice). This separation can be varied from 12 down to 3 μm. The advantage of variable spacing is that we can load a three-dimensional (3D) shaped cloud into a single layer of the 2D pancakes at maximum separation and then compress the pancake adiabatically to reach a deep 2D regime. The maximum vertical confinement can reach more than 20 kHz and we optimize it at 1 kHz to observe moiré pattern and superfluid of ultracold atoms.

The twisted-bilayer optical lattices are created by two sets of 2D square lattice V_1 and V_2. A twisted angle of $\theta=5.21°$ is set between the two lattice potentials, namely, $V_2(r)=V_1(Sr)$, $S=\begin{pmatrix}\cos\theta & -\sin\theta\\ \sin\theta & \cos\theta\end{pmatrix}$. The optical lattices V_1 and V_2 are derived from two continuous-wave Ti:sapphire single frequency lasers (M Squared lasers SolsTiS and Coherent MBR-110), respectively. Two lattice beams V_{1x} and V_{1y} of V_1 are frequency-shifted +80 and +95 MHz by two single-pass acousto-optic modulators, respectively. The same applies to the two lattice beams V_{2x} and V_{2y} of lattice V_2. The four lattice beams are coupled into polarization-maintaining single-mode fibres to improve the stability of the beam pointing and achieve better beam-profile quality. After the fibres, each lattice beam is focused by a lens and retroreflected by a concave mirror. To generate the vector light shift, we use the same circular polarization for two lattice beams to produce spatial intensity modulation. In the experiment, we can determine and calibrate this angle by measuring the intersection angle between two lasers and the moiré period from the in situ images. The estimated uncertainty of the two methods is about 0.05°.

We use the MW field to couple the two spin states for manipulating the interlayer coupling. The 6.8 GHz MW signal is amplified by a 10 W solid state amplifier (Kuhne Electronic, KU PA 640720-10A). We place a circulator on the output of the amplifier to reduce reflected power coming back to the amplifier. The MW is emitted out to the atoms by a sawed-off waveguide, which is placed outside the high vacuum glass cell. We use MW cables to transfer MW from the amplifier to the waveguide. With this MW power amplifier, we can reach the maximum interlayer coupling strength of about $1.0E_r$. It is feasible to increase the interlayer coupling strength to about several E_r by using an available higher power amplifier.

Our image system consists of an objective with a numerical aperture of 0.69, working distance of 11 mm and effective focal length of 18 mm. A 900 mm lens after the objective leads to a magnification of ×50 for in situ imaging with an EMCCD (Andor iXon Ultra 897). We also use a 200 mm (400 mm) lens after the objective leads to a magnification of ×11 (22) for the TOF absorption imaging with 18 ms. The atoms are detected by state-selective absorptive imaging. As we choose two ground hyperfine Zeeman states of ^{87}Rb $|F=2, m_F=0\rangle$ of the $F=2$, and $|F=1, m_F=1\rangle$ of the $F=1$ hyperfine manifold as the two internal spin states, we can fully resolve the population in each individual state. For $|F=2, m_F=0\rangle$ state, a 50 μs long imaging pulse of resonant light on the $F=2\rightarrow F'=3$ D_2 cycling transition is used to detect the $|2\rangle$ atoms. To detect the $|F=1, m_F=1\rangle$ state, a resonant light pulse on the $F=2\rightarrow F'=3$ cycling transition is first used to remove the $|2\rangle$ atoms and then a 50 μs long imaging pulse of resonant light on the $F=2\rightarrow F'=3$ is applied at the same time with a repump light (resonant light $F=1\rightarrow F'=2$) to detect the $|1\rangle$ atoms.

When studying the superfluid to MI transition, we use the standard method of interference pattern contrast (visibility) to show this transition[37,44]. We first load the atoms in state $|1\rangle$ into the lowest *s* band of lattice V_1 by ramping up V_1 and V_2 simultaneously with 30 ms, and then ramp up the MW field with 10 ms to drive the transition from $|1, S\rangle$ to $|2, S\rangle$. The atoms are detected by state-selective absorptive imaging with TOF of 18 ms after switching off all lattices and trapping light. In experiment, we first check that BEC is still kept (Extended Data Fig. 1) as ramp up the lattice V_1 (or V_2) to the higher lattice depth than $24E_r$ and then ramp down again, which makes sure to perform the phase transition from SF to MI successfully for the lattice V1 (or V2). When adding the interlayer coupling between two spin states, and at the same time a quasi-disorder is introduced, there are two more mechanics to make the system not completely reversible. One is the finite coherent time between two spin states. When the system is prepared initially in the spin down, the system will become the spin mixture after the interlayer coupling is ramped back down. We define this process as irreversibility. The other is that adiabaticity is broken down by a quasi-period or disordered lattice, which induces not to completely remain in the zero-momentum state after ramping the lattices back down.

Tune-out wavelength for twisted-bilayer optical lattices

The a.c. Stark shift, or light shift, is a light-induced change of energy level. For alkali-metal atoms, the total a.c. Stark shift can be expressed in the irreducible components (including scalar, vector and tensor components) of the polarizability[45]:

$$\begin{aligned}\Delta U &= \Delta U(F, m_F; \omega)\\ &= -I\left[\alpha^{(0)}(\omega)+\alpha^{(1)}(\omega)(\xi\mathbf{e}_k\cdot\mathbf{e}_B)\frac{m_F}{F}\right.\\ &\quad\left.+\alpha^{(2)}(\omega)\frac{3\cos^2\phi-1}{2}\frac{3m_F^2-F(F+1)}{F(2F-1)}\right],\end{aligned} \tag{2}$$

where F is the total atomic angular momentum, m_F is the magnetic quantum number, ω is the laser frequency, I is the laser field intensity, ξ is light ellipticity, $\mathbf{e}_k$ and $\mathbf{e}_B$ are unit vectors along the light wave vector and magnetic field quantization axis, respectively, and ϕ is the intersection angle between the linearly polarized component of light field and $\mathbf{e}_B$. This formula comes from the perturbation expansion. Note that the range of values of light ellipticity is $\xi\in[-1,1]$, $\xi=\pm1$ denotes left and right circular polarization. $\alpha^{(0)}(\omega)$, $\alpha^{(1)}(\omega)$, $\alpha^{(2)}(\omega)$ are the scalar, vector and tensor polarizability, respectively. Scalar shift is spin independent. Vector shift acts like an effective magnetic field to generate the linear Zeeman splitting (light shift proportional to m_F), which depends on the ellipticity of the light and the intersection angle between the laser beam wave vector and magnetic field quantization axis $\mathbf{e}_B$. So, there are two methods to control the vector shift: rotating bias magnetic field and changing light polarization. The tensor part is derived from the linearly polarized light and acts as an effective d.c. electric field.

For the first excited state of alkali-metal atoms, the fine structure interaction induces the spectral lines of the D1 ($5^2S_{1/2}\rightarrow5^2P_{1/2}$) and D2 ($5^2S_{1/2}\rightarrow5^2P_{3/2}$) lines. The coefficients of the scalar, vector and tensor shifts of the ground states $5^2S_{1/2}$ of ^{87}Rb atoms in equation (2) are given by

$$\begin{aligned}\alpha^{(0)}(\omega) &\approx -\frac{\pi c^2\Gamma_{D2}}{2\omega_0^3}\left(\frac{2}{\delta_{D2}}+\frac{1}{\delta_{D1}}\right),\\ \alpha^{(1)}(\omega) &\approx -\frac{\pi c^2\Gamma_{D2}}{2\omega_0^3}\left(\frac{1}{\delta_{D2}}-\frac{1}{\delta_{D1}}\right)g_F F,\\ \alpha^{(2)}(\omega) &\approx 0,\end{aligned} \tag{3}$$

where Γ_{D_2} is the decay rate of the excited state for D_2 line, $\omega_0 = \frac{1}{3}\omega_{D1} + \frac{2}{3}\omega_{D2}$ is the effective frequency, $\delta_{D_1} = \omega - \omega_{D1}$, $\delta_{D_2} = \omega - \omega_{D2}$ is the frequency detuning of the laser. Therefore, according to equation (3) we only consider the scalar and vector shift in this work. We use tune-out wavelength for spin-dependent optical lattice, in which a.c. Stark shifts cancel. Two internal spin states have different tune-out wavelengths when the contributions of both the scalar and vector shifts are included[35].

We choose two ground hyperfine Zeeman states of ^{87}Rb $|F = 2, m_F = 0\rangle$ of the $F = 2$, and $|F = 1, m_F = 1\rangle$ of the $F = 1$ hyperfine manifold as the two internal spin states. A bias magnetic field with 10 Gauss is applied along the 45° diagonal line of the square lattice V_2. We scan the wavelength of the optical lattice beams to determine the tune-out wavelength precisely, as shown in Extended Data Fig. 2. The tune-out wavelength for $|1, 1\rangle$ state is determined at 788.28 nm with σ_- circular polarization as shown in Extended Data Fig. 2c, which balances the contribution of the scalar and vector shift. Thus, we choose this wavelength for the lattice V_2. Note that the tune-out wavelength for $|1, 1\rangle$ state is sensitive to the intersection angle between the laser beam wave vector and magnetic field quantization axis, which requires a careful alignment of the bias magnetic field. The spin state $|2, 0\rangle$ only experiences the square lattice V_2 with the red-detuning a.c. stark shift (which is only from scalar shift), as shown in Extended Data Fig. 2d,f; by contrast, the spin state $|1, 1\rangle$ experiences no shift.

On the other hand, there is only the contribution of the scalar shift for the spin state $|2, 0\rangle$; the tune-out wavelength for $|2, 0\rangle$ state is 790.02 nm as shown in Extended Data Fig. 2a, which is well known and studied experimentally[34,35]. We choose this tune-out wavelength of 790.02 nm with σ_+ circular polarization as the wavelength of the lattice V_1. Thus, the spin state $|1, 1\rangle$ experiences the square lattice V_1 with the red-detuned a.c. stark shift. By contrast, the spin state $|2, 0\rangle$ sees zero light shift. Note that the tune-out wavelength for $|2, 0\rangle$ state is insensitive to the intersection angle between the laser beam wave vector and magnetic field quantization axis. The spin state $|1, 1\rangle$, however, has a different lattice depth in two orthogonal directions of the lattice V_1, respectively, and feels the lattice V_1 with the red-detuning a.c. stark shift (which is only from vector shift at the wavelength of 790.02 nm) as shown in Extended Data Fig. 2b,e.

A moiré superlattice can be generated by a small difference in lattice constant or orientation. Because two different wavelengths are used for twisted-bilayer lattices in this work, there is a large-period superlattice with $\Delta\lambda = 179$ μm, much larger than the size of atomic cloud. Therefore, we can adjust the retroreflected concave mirror to load atoms into the lower potential well of the long-period superlattice and neglect the influence on the measurement of moiré pattern. In the future, we can correct this effect of two different wavelengths by using a slight angle lattice beam for V_2 to ensure the same lattice constant for two lattice potentials.

Band structures and flat band

For square lattices, the commensurate angles θ satisfy $\tan(\theta/2) = \bar{m}/\bar{n}$, where $\bar{m}$ and $\bar{n}$ are coprime natural number. An equivalent condition is $\cos\theta = \bar{a}/\bar{c}$ and $\sin\theta = \bar{b}/\bar{c}$, which can be defined by Pythagorean triples $(\bar{a}^2 + \bar{b}^2 = \bar{c}^2$, where $(\bar{a}, \bar{b}, \bar{c}) \in N$ are positive integers)[13]. The relationship between $(\bar{m}, \bar{n})$ and $(\bar{a}, \bar{b}, \bar{c})$ is $(\bar{m} + i\bar{n})^2 = (\bar{a} + i\bar{b})$ when $(\bar{m} + \bar{n}) \in$ odd and $(\bar{m} + i\bar{n})^2 = 2(\bar{a} + i\bar{b})$ when $(\bar{m} + \bar{n}) \in$ even. For the commensurate optical lattice, the period of its supercell (sc) is given by $\lambda_{sc} = \bar{m}a/\sin(\theta/2) = 2\bar{m}\lambda_{mo}$ when $(\bar{m} + \bar{n}) \in$ odd and $\lambda_{sc} = \bar{m}a/\sin(\theta/2) = \sqrt{2}\,\bar{m}\lambda_{mo}$ when $(\bar{m} + \bar{n}) \in$ even.

Here, we choose the band structure of the commensurate optical lattice with the commensurate angle $\theta = 2\arctan(1/22)$ as an approximation of the experimental case. If getting a better approximation of band structure for the experimental case, we can choose the larger supercell to calculate the energy band structure, whose commensurate angle is closer to the experimental case. The band structure $E(\mathbf{k})$ of the commensurate optical lattice can be obtained by solving the stationary Schrödinger equation, $H\Psi = E\Psi$, with the Bloch function, $\Psi(\mathbf{r}) = \exp^{i\mathbf{k}\cdot\mathbf{r}}u(\mathbf{r})$. Here the Hamiltonian H is given as

$$H = \begin{pmatrix} -\frac{\hbar^2}{2m}\nabla^2 + V_1 + \frac{\Delta}{2} & \Omega_R \\ \Omega_R & -\frac{\hbar^2}{2m}\nabla^2 + V_2 - \frac{\Delta}{2} \end{pmatrix}, \tag{4}$$

$u(\mathbf{r})$ is a periodic function with the same periodicity as the coupled lattice. The spin-dependent square optical lattice with a twist angle θ can be described by the potentials

$$\begin{aligned} V_1 &= V_0\left[\sin^2\left(kx\cos\frac{\theta}{2} - ky\sin\frac{\theta}{2}\right) + \sin^2\left(ky\cos\frac{\theta}{2} + kx\sin\frac{\theta}{2}\right)\right], \\ V_2 &= V_0\left[\sin^2\left(kx\cos\frac{\theta}{2} + ky\sin\frac{\theta}{2}\right) + \sin^2\left(ky\cos\frac{\theta}{2} - kx\sin\frac{\theta}{2}\right)\right], \end{aligned} \tag{5}$$

where $k = 2\pi/\lambda$ is the wave number of lasers for the lattice and V_0 describes the lattice depth. In numerics, we first discretize the unit supercell of area $\sqrt{\bar{c}}a \times \sqrt{\bar{c}}a$ in real space ($\bar{c}$ is the largest value in the Pythagorean triple) into $l \times l$ grids, and then diagonalize the effective Hamiltonian for $u(\mathbf{r})$. As shown in Extended Data Fig. 3, the band structure approaches the flat band when increasing the interlayer coupling.

As our system allows for flexible control of the interlayer couplings, the flat band in the lowest energy band can be realized. The Hamiltonian equation (4) can be formally diagonalized as

$$H = \begin{pmatrix} H^+_{\text{eff}} & 0 \\ 0 & H^-_{\text{eff}} \end{pmatrix}, \tag{6}$$

where

$$H^{\pm}_{\text{eff}} = h_0 \pm h_1, \tag{7}$$

with $h_0 = -\frac{\hbar^2}{2m}\nabla^2 + \frac{V_1 + V_2}{2}$, and $h_1 = \sqrt{\Omega_R^2 + \frac{(V_1 - V_2 + \Delta)^2}{4}}$. In the large interlayer coupling limit, $\Omega_R \gg V_0, \Delta$, the low-energy band structure is encoded in the effective Hamiltonian H^-_{eff} in the lower-right block, which can be further approximated as

$$H^-_{\text{eff}} \approx -\frac{\hbar^2}{2m}\nabla^2 + \frac{V_1 + V_2}{2} - \frac{(V_1 - V_2 + \Delta)^2}{8\Omega_R} - \Omega_R, \tag{8}$$

or in a rougher way

$$H^-_{\text{eff}} \approx -\frac{\hbar^2}{2m}\nabla^2 + \frac{V_1 + V_2}{2} - \Omega_R, \tag{9}$$

The approximated effective Hamiltonians correspond to some effective lattices for a single-layer (single-component) system, separately, $V = \frac{V_1 + V_2}{2} - \frac{(V_1 - V_2 + \Delta)^2}{8\Omega_R}$ for equation (8), and $V = \frac{V_1 + V_2}{2}$ for equation (9), with certain global energy shift. Specifically, equation (9) indicates that the system becomes the single layer (single-component) experiencing a twisted optical lattice.

When increasing the interlayer coupling into the strong region, the long-wavelength moiré potential becomes deeper, so atoms in the lowest band are isolated on a larger spatial scale (moiré wavelength), which enhances the wave function localization and contributes to the creation of a flat band. The single-layer system with a twisted optical lattice (approximation at the strong interlayer coupling limit) admits a flat-band structure in the lowest band, which has been studied experimentally in photonic system[13–15]. The moiré flat bands have several advantages.

First, the flat bands quench kinetic energy scales (wave function localization), thereby drastically enhance the role of interactions and amplify the effects of interactions. Second, the moiré superlattice leads to the emergence of minibands within a reduced Brillouin zone. The small Brillouin zone means that low atomic densities are sufficient for full filling or depletion of the superlattice bands, which is easily controlled in an experiment.

Theoretical calculation of the modified superfluid to insulator transition

In the mean-field approximation, the system for the superfluid phase can be well described by the coupled Gross–Pitaevskii (GP) equations

$$\begin{aligned} i\hbar\frac{\partial\psi_1}{\partial t} &= \left[-\frac{\hbar^2}{2m}\nabla^2+\frac{1}{2}m\omega_\perp^2(x^2+y^2)+V_1+\eta g_{11}|\psi_1|^2+\eta g_{12}|\psi_2|^2\right]\\ &\quad \psi_1+\hbar\Omega_R\psi_2,\\ i\hbar\frac{\partial\psi_2}{\partial t} &= \left[-\frac{\hbar^2}{2m}\nabla^2+\frac{1}{2}m\omega_\perp^2(x^2+y^2)+V_2+\eta g_{12}|\psi_1|^2+\eta g_{22}|\psi_2|^2\right]\\ &\quad \psi_2+\hbar\Omega_R\psi_1, \end{aligned} \tag{10}$$

where the MW detuning is $\Delta = 0$ and the wave function is normalized as $\sum_i\int|\psi_i|^2\mathrm{d}\mathbf{r} = N$, with N the total atom number. The strong confinement along the z axis gives rise to the quasi-2D interaction strengths represented by a reduction coefficient η multiplied by $g_{ij} = 4\pi\hbar^2 a_{ij}/m$, where $\eta^{-1} = \sqrt{h/m\omega_z}$ defines the characteristic length along the z axis and a_{ij} is the 3D s-wave scattering length. In the experiment, the trapping frequency $\omega_z \cong 2\pi\times 1$ kHz, and the scattering length for the ^{87}Rb atoms is about $a_{ij}\cong 100a_B$ with a_B the Bohr radius. This indicates that even though the system is thermodynamically 2D, the collisions still keep their 3D character with $\eta^{-1}\gg a_{ij}$. Considering the similarity in scattering lengths a_{11}, a_{22} and a_{12} for the ^{87}Rb atoms, in the calculation we focus on the SU(2) symmetric interaction with $g = g_{11} = g_{22} = g_{12}$. In addition to the intercomponent atomic interaction, the two components are also coupled by a MW pulse, which causes Rabi oscillations with the frequency Ω_R.

By using the imaginary time evolution method, one can solve the GP equations numerically for the ground states in the harmonic trap. Theoretically, the non-commensurate twist angle $\theta = 5.21°$ should be a localized single particle ground state whereas the commensurate angle $\theta = 2\arctan\frac{1}{22}$ gives rise to extended ground states in the absence of interactions. Experimentally, the interatomic interaction is dominant, and always leads to extended many-body states with the aperiodic and periodic bilayer lattices becoming almost indistinguishable.

The phase transition from superfluid to MI can be well described by the Bose–Hubbard model in the tight-binding approximation. For simplicity we consider the interlayer coupling as a quasi-periodically perturbed potential, which leads to a site-dependent energy offset

$$M_i = M_R[\sin^2(i_x\pi\cos\theta + i_y\pi\sin\theta) + \sin^2(i_y\pi\cos\theta - i_x\pi\sin\theta)], \tag{11}$$

where the subindex i_x and i_y label the position of the ith site in the two-dimensional space. The tight-binding Hamiltonian for one layer then is given by

$$H = -t\sum_{\langle i,j\rangle} b_i^\dagger b_j + \frac{U}{2}\sum_i \hat{n}_i(\hat{n}_i-1) + \sum_i (M_i-\mu)\hat{n}_i, \tag{12}$$

where the first term describes the nearest-neighbour tunnelling with $b^\dagger$ and b being the creation and annihilation operators, and the second term represents the on-site interaction. The hopping amplitude t is considered to be site-independent for weak interlayer coupling and can be estimated by $t = \frac{4}{\sqrt{\pi}}E_r(V_0/E_r)^{3/4}e^{-2(V_0/E_r)^{1/2}}$. The local repulsion U depends on the depth of the optical lattice, and is given by $U = \sqrt{8/\pi}ka_sE_r(V_0/E_r)^{3/4}$ (ref. [46]). The chemical potential μ controls the average number of atoms in the moiré lattice.

The mean-field phase diagram (Fig. 5a) can be mapped by using the Gutzwiller method, which expands the local state $|\psi_i\rangle$ at site i in the Fock basis[47,48]. When the interlayer coupling $M_i = 0$, the system is reduced to the standard Bose–Hubbard model[38], which includes two phases, the superfluid phase and the MI phase[44,49]. While the superfluid phase is identified by the superfluid order parameter $\langle\hat{b}_i\rangle \neq 0$ and an arbitrary filling of the atoms on the site, the MI phase emerges with an integer number of atoms per site with $\langle\hat{b}_i\rangle = 0$. When the interlayer coupling $M_i \neq 0$, the persistent coherence of the moiré and primary lattice length scale as well as density distribution in real space can be used to distinguish the phases, which is determined by the order parameter $\langle\hat{b}_i\rangle$ and the filling of the atoms on the site n as shown in Extended Data Fig. 4. The chemical potential $\mu/U = 1$ is considered in this calculation.

Phase diagram with zero temperature and the homogeneous system is predicted theoretically as shown in Extended Data Fig. 4a, in which four phases of superfluid (SF), superfluid II (SF-II), MI and insulator (I) are included. The SF-II phase is a state with superfluid domains embedded in a gapped insulate state, which is caused by interlayer coupling. So, the SF-II phase can be identified by checking the disappearance of the moiré-scale long-range correlation with vanishing moiré lattice momentum but the short-range coherence with residual primary lattice momentum remains. At the same time, the SF-II phase supports the moiré pattern in the real space. As MI is an incompressible insulator for integer filling factor with a gap U for particle-hole excitations induced by the on-site interaction U, the moiré pattern in the real space appears only when the interlayer coupling strength is larger than U to break this gap. Therefore, the I phase supports the moiré pattern in the real space and no spatial coherence at all scales, which approaches the MI phase without the moiré pattern in the real space in the limit of weak interlayer coupling. Here, the phase transition between the SF to the MI phase should have an intermediate phase SF-II. Obviously, the coherence is lost almost simultaneously in all length scales at the critical point at very weak interlayer coupling only for zero temperature as shown in Fig. 5a. By contrast, at finite temperature, the thermodynamic quantities behave smoothly near the critical point and more long-range moiré coherence is lost before the short-range primary lattice length. Therefore, there exists an SF-MI critical regime, which seems likely to be a thermodynamic phase and is not predicted theoretically at zero temperature. The SF-MI critical regime has the same coherence as SF-II without the moiré-scale long-range correlation but with the short-range coherence. However, the SF-MI critical regime does not support the moiré pattern in real space that is distinguished from SF-II. In fact, the insulator phase presents special characteristics due to the strong interaction and quasi-disorder induced by the larger interlayer coupling, similar to a Bose glass insulator from the model of a disordered strongly interacting bosonic system[38–40].

Data availability

All data generated or analysed during this study are included in this published article. Further data are also available from the corresponding authors upon reasonable request.

43. Xiong, D., Wang, P., Fu, Z., Chai, S. & Zhang, J. Evaporative cooling of ^{87}Rb atoms into Bose-Einstein condensate in an optical dipole trap. *Chin. Opt. Lett.* **8**, 627–629 (2010).
44. Greiner, M., Mandel, O., Esslinger, T., Hänsch, T. W. & Bloch, I. Quantum phase transition from a superfluid to a Mott insulator in a gas of ultracold atoms. *Nature* **415**, 39 (2002).
45. Steck, D. A. *Quantum and Atom Optics* https://atomoptics.uoregon.edu/~dsteck/teaching/quantum-optics/ (2007).
46. Zwerger, W. Mott Hubbard transition of cold atoms in optical lattices. *J. Opt. B: Quantum Semiclass. Opt.* **5**, S9–S16 (2003).
47. Krauth, W., Caffarel, M. & Bouchaud, J. P. Gutzwiller wave function for a model of strongly interacting bosons. *Phys. Rev. B* **45**, 3137–3140 (1992).

48. Sheshadri, K., Krishnamurthy, H. R., Pandit, R. & Ramakrishnan, T. V. Superfluid and insulating phases in an interacting-Boson model: mean-field theory and the RPA. *Europhys. Lett.* **22**, 257–263 (1993).
49. Jaksch, D., Bruder, C., Cirac, J. I., Gardiner, C. W. & Zoller, P. Cold Bosonic atoms in optical lattices. *Phys. Rev. Lett.* **81**, 3108–3111 (1998).

Acknowledgements This research is supported by Innovation Program for Quantum Science and Technology (grant no. 2021ZD0302003), National Key Research and Development Program of China (grant nos. 2016YFA0301602, 2018YFA0307601 and 2022YFA1404101), NSFC (grant nos. 12034011, 12022406, 12074342 and 11804203), the Fund for Shanxi '1331 Project' Key Subjects Construction and Tencent (Xplorer Prize). C.C. acknowledges support by the National Science Foundation (grant no. PHY-2103542) and the Army Research Office STIR (grant no. W911NF2110108).

Author contributions J.Z. conceived the idea and performed the experimental designs. L.W., Z.M., F.L., K.W., P.W. and J.Z. performed the experiments. C.C., Z.M., L.W., F.L., W.H. and J.Z. analysed the data and all authors discussed the results. W.H., C.G. and J.Z. performed the simulation. Z.M. plotted the figures. J.Z. and C.C. wrote the manuscript. All authors interpreted the results and reviewed the manuscript. J.Z. designed and supervised the project.

Competing interests The authors declare no competing interests.

Additional information

Correspondence and requests for materials should be addressed to Jing Zhang.

Peer review information *Nature* thanks Richard Schmidt and the other, anonymous, reviewer(s) for their contribution to the peer review of this work.

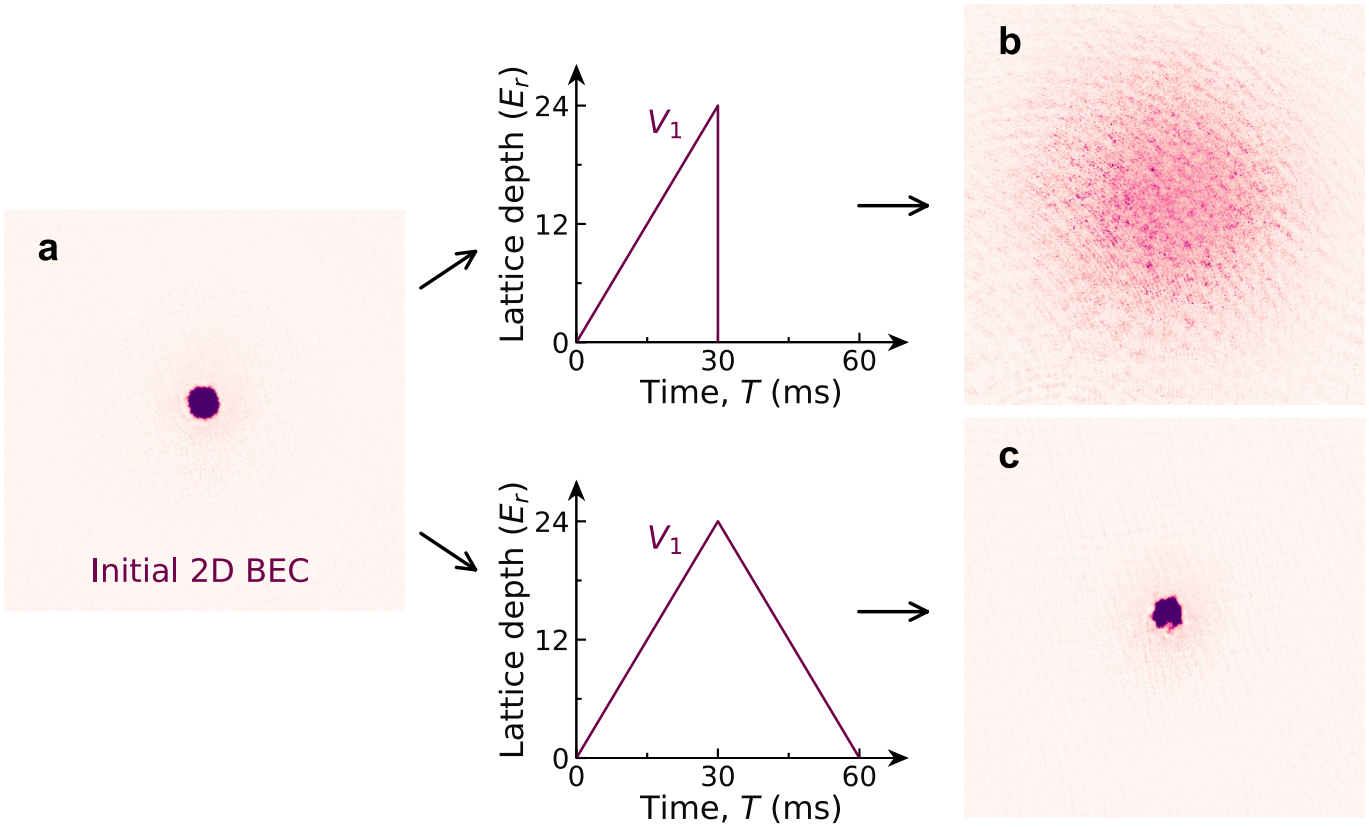

Extended Data Fig. 1 | Coherence in the SF-MI transition. a, The initial BEC in 2D pancake-like potential. **b**, Absorption image after atoms are released abruptly from an optical lattice potential V_1 (or V_2) with a potential depth $24E_r$. **c**, Absorption image when the lattice is ramped up to the lattice depth $24E_r$ and then ramp down to zero. The images are obtained after 18 ms free space expansion.

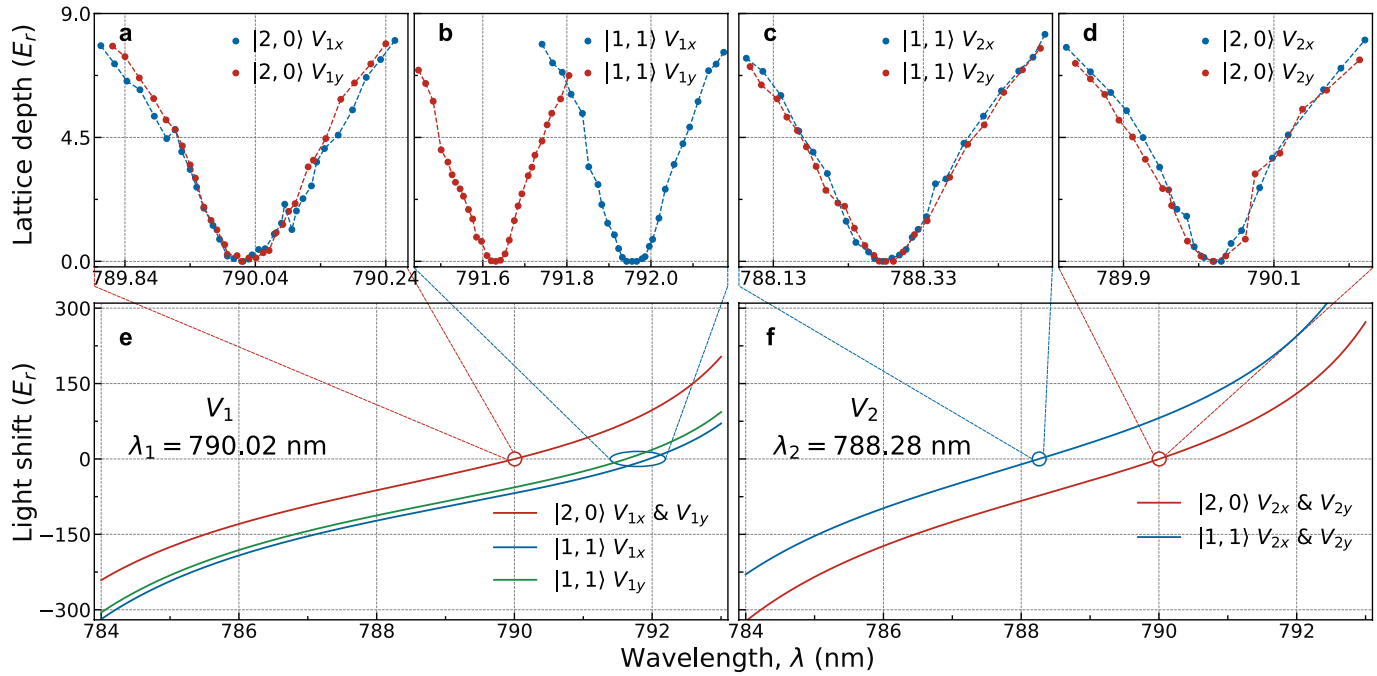

Extended Data Fig. 2 | Determination of tune-out wavelengths. a–**b**, The lattice depth V_{1x} (blue) and V_{1y} (red) as a function of wavelength λ for the two different hyperfine states $|F=1, m_F=1\rangle$ and $|F=2, m_F=0\rangle$. The angles between V_{1x}, V_{1y} and B_0 are 39.79° and 50.21° respectively. **c**–**d**, The potential depth V_{2x} (blue) and V_{2y} (red) as a function of wavelength λ for the two different hyperfine states $|F=1, m_F=1\rangle$ and $|F=2, m_F=0\rangle$. **e**, Theoretical light shift of V_{1x}, V_{1y} for $|1,1\rangle$ and $|2,0\rangle$. **f**, Theoretical lattice depth of V_{2x}, V_{2y} for $|1,1\rangle$ and $|2,0\rangle$. The bias magnetic field of 10 Gauss is applied along the 45° diagonal line of the square lattice V_2.

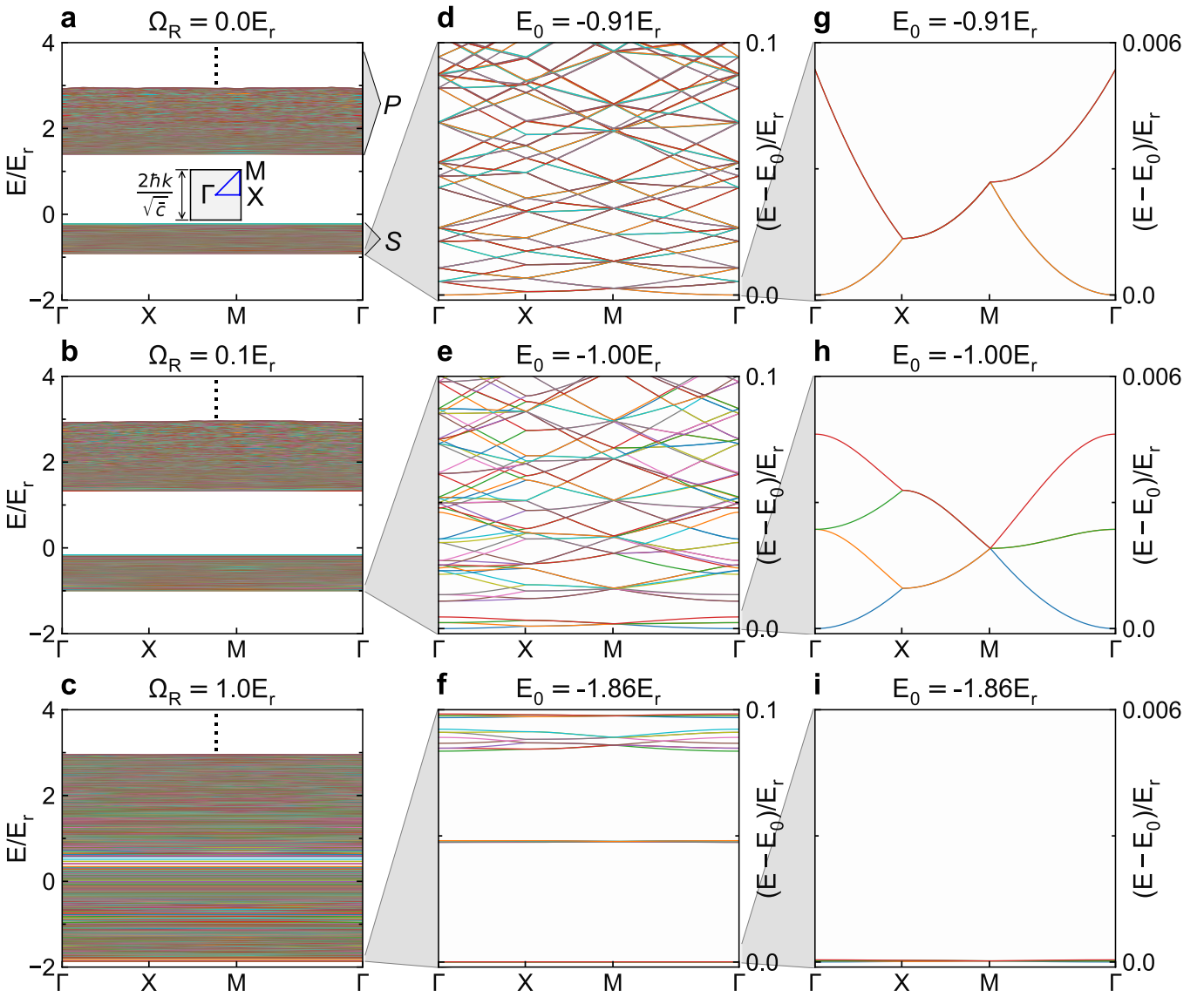

Extended Data Fig. 3 | Band structure of the twisted-bilayer optical lattices. The twist angle of the commensurate optical lattice is $\theta = 2\arctan(1/22)$, whose band structure is regarded as an approximation of the experimental case $\theta = 5.21^\circ$. **a**, **b** and **c** show the band structures for the interlayer coupling strength $\Omega_R = 0E_r$, $0.1E_r$ and $1E_r$ respectively. **a** also gives the band structure without the interlayer coupling in the form of the superlattice minibands within the same reduced Brillouin zone. **d**, **e** and **f** are the enlargement of the lowest bands of **a**, **b**, and **c**, respectively. **g**, **h** and **i** are the further enlargement of the lowest bands of **d**, **e** and **f**, respectively. Here, the MW detuning is $\Delta = 0$, $V_0 = 4E_r$ and E_0 corresponds to the energy of the lowest band.

a

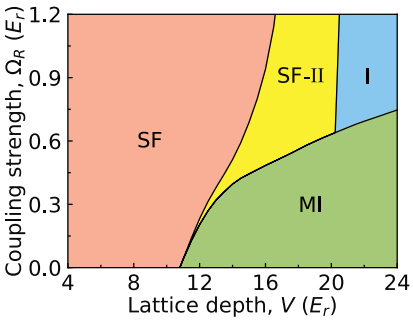

b

	Real space	Momentum space	
	Moiré pattern	Coherence at the primary lattice length-scale	Coherence at the moiré length-scale
SF	Yes	Yes	Yes
SF-II	Yes	Yes	No
I	Yes	No	No
MI	No	No	No

c

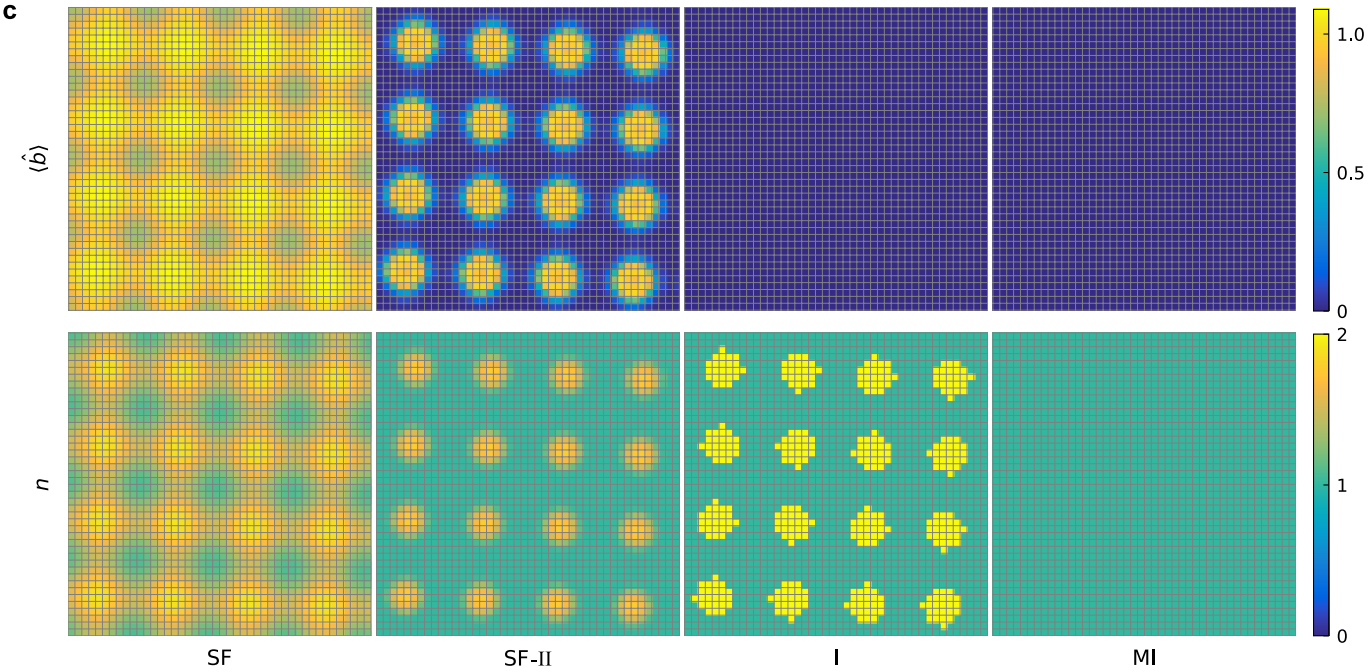

Extended Data Fig. 4 | Characteristics of the different phases. a, Phase diagram, where SF, SF-II, MI, and I refer to superfluid, superfluid only with short-range coherence, Mott insulator, and insulator. **b**, Table shows the features of the different phases. **c**, Plots of the order parameter $\langle \hat{b}_i \rangle$ and the filling of the atoms on the site n for the different phases. Parameters (V/E_r, Ω_R/E_r) are (10,0.6), (15,0.6), (23,0.3) and (23,1.1) for the plots from left to right respectively. The chemical potential $\mu/U = 1$ is considered.